NANO · MICRO small
www.small-journal.com

Synthesis and Nanostructure Investigation of Hybrid β-Ga_2O_3/$ZnGa_2O_4$ Nanocomposite Networks with Narrow-Band Green Luminescence and High Initial Electrochemical Capacity

Niklas Wolff, Tudor Braniste, Helge Krüger, Sebastian Mangelsen, Md Redwanul Islam, Ulrich Schürmann, Lena M. Saure, Fabian Schütt, Sandra Hansen, Huayna Terraschke, Rainer Adelung, Ion Tiginyanu,* and Lorenz Kienle**

The material design of functional "aero"-networks offers a facile approach to optical, catalytical, or and electrochemical applications based on multiscale morphologies, high large reactive area, and prominent material diversity. Here in this paper, the synthesis and structural characterization of a hybrid β-Ga_2O_3/$ZnGa_2O_4$ nanocomposite aero-network are presented. The nanocomposite networks are studied on multiscale with respect to their micro- and nanostructure by X-ray diffraction (XRD) and transmission electron microscopy (TEM) and are characterized for their photoluminescent response to UV light excitation and their electrochemical performance with Li-ion conversion reaction. The structural investigations reveal the simultaneous transformation of the precursor aero-GaN(ZnO) network into hollow architectures composed of β-Ga_2O_3 and $ZnGa_2O_4$ nanocrystals with a phase ratio of ≈1:2. The photoluminescence of hybrid aero-β-Ga_2O_3/$ZnGa_2O_4$ nanocomposite networks demonstrates narrow band (λ_{em} = 504 nm) green light emission of $ZnGa_2O_4$ under UV light excitation (λ_{ex} = 300 nm). The evaluation of the metal-oxide network performance for electrochemical application for Li-ion batteries shows high initial capacities of ≈714 mAh g^{-1} at 100 mA g^{-1} paired with exceptional rate performance even at high current densities of 4 A g^{-1} with 347 mAh g^{-1}. This study provides is an exciting showcase example of novel networked materials and demonstrates the opportunities of tailored micro-/nanostructures for diverse applications a diversity of possible applications.

1. Introduction

In the past, significant research effort has been devoted to the design, fabrication, and characterization of engineered hollow nanomaterial structures to examine new functionalities based on their high-surface area.[1–3] Such hollow micro- and nanostructures introduce well-defined geometrical boundaries and meso- to nanoscale open volumes to allow for hierarchical material architectures with increasing compositional and morphological design complexity, especially in the field of metal oxides.[4,5] Their structural features, such as a low density and high surface to volume ratio, as well as permeable and porous shells, promote many unique physiochemical properties advertising complex hollow nanostructures for energy-related applications including storage and conversion,[6–9] catalysis,[10,11] gas sensing[12,13] or biomedical applications.[14] Among this class of hollow material structures, highly porous and ultra-lightweight 3D networks

N. Wolff, M. R. Islam, U. Schürmann, L. Kienle
Synthesis and Real Structure
Department of Material Science
Kiel University
Kaiserstraße 2 D-24143, Kiel, Germany
E-mail: niwo@tf.uni-kiel.de; lk@tf.uni-kiel.de

N. Wolff, S. Mangelsen, U. Schürmann, F. Schütt, S. Hansen, H. Terraschke, R. Adelung, L. Kienle
Kiel Nano
Surface and Interface Science (KiNSIS)
Kiel University
Christian-Albrechts-Platz 4 D-24118, Kiel, Germany

The ORCID identification number(s) for the author(s) of this article can be found under https://doi.org/10.1002/smll.202207492.

DOI: 10.1002/smll.202207492

T. Braniste, I. Tiginyanu
National Center for Materials Study and Testing
Technical University of Moldova
Stefan cel Mare 168, Chisinau MD-2004, Moldova
E-mail: ion.tighineanu@cnstm.utm.md

H. Krüger, L. M. Saure, F. Schütt, S. Hansen, R. Adelung
Functional Nanomaterials
Department of Material Science
Kiel University
Kaiserstraße 2 D-24143, Kiel, Germany

S. Mangelsen, H. Terraschke
Solid State Chemistry and Catalysis
Department of Inorganic Chemistry
Kiel University
Max-Eyth-Straße 2 D-24118, Kiel, Germany

I. Tiginyanu
Academy of Sciences of Moldova
Stefan cel Mare av. 1, Chisinau MD-2001, Moldova

offer outstanding high surface to volume ratios and design flexibility for diverse functionalities.[15–19]

In this respect, interpenetrating sacrificial tetrapodal ZnO (T-ZnO) networks provide a rigid framework encouraging the design of hollow-tube "aero"-networks with tailored porosities of 50–94% and variable densities of < 2–5 mg cm^{-3} offering high functionality and functionalization capabilities. The introduced template approach successfully interconnects nanoscopic physical phenomena of microscale building units to the macroscale, which is required for many applications. The high diversity of this approach opens up a vast exploration space in which manifold functional aero-materials based, for example, on carbon species, metal nitrides or glass and polymers are under investigation. Up to date, numerous reports include aero-networks based on carbon species, for example, aero-graphite[20] and aero-graphene[18,21] nitride materials such as aero-GaN(ZnO)[22,23] and aero-BN[24] and many others including aero-Si,[25] aero-ZnS[26] and aero-Ga_2O_3.[27] Further, their modifications by functionalization with metallic nanoparticles during and after the synthesis have been demonstrated to improve the catalytic performance.[28,29] A wide range of possible applications becomes possible from microfluidics and pneumatic systems[18] to optical light diffusion[24] or photocatalysis[28,29] and can be extended to bio-scaffolds and hydrogel templates as well as supercapacitor structures.[30] This heterogeneity in the material selection and associated properties is driving fundamental research to identify fabrication routes and new applications of new ultralight weight and porous aero-networks.

In this work, a gallium oxide based aero-network structure containing the spinel-type phase zinc gallate ($ZnGa_2O_4$) as a majority component is developed based on the simple high-temperature oxidation of aero-GaN(ZnO).[23] Like β-Ga_2O_3, $ZnGa_2O_4$ belongs to the group of ultra-wide bandgap oxide semiconductors exhibiting a bandgap of 4.6–5.2 eV, paired with high chemical and thermal stability.[31–33] Therefore gallium oxide phases, especially $ZnGa_2O_4$, are investigated for their photocatalytic applications or as gas sensors.[34–36] For in-depth information on $ZnGa_2O_4$, the reader is referred to a review by Chen et al. highlighting all aspects from synthesis to applications.[37]

$ZnGa_2O_4$ crystallizes in the normal spinel-type structure ($Fd\bar{3}m$), in which octahedral sites are occupied by Ga, forming a network of edge-sharing GaO_6 octahedra, like in β-Ga_2O_3, and tetrahedral sites occupied by Zn. Due to their intrinsic band structure, phase pure $ZnGa_2O_4$ nanoparticle systems have been studied as platform for optoelectronic applications showing prominent phosphorescence of blue emission under ultraviolet (UV, λ = 254 nm) light excitation.[33] The emission spectrum can be tailored by introducing dopants on the tetrahedral sites of the host-lattice with rare earth[38] metal or Mn^{2+}, or Cr^{3+} ions[39] to achieve green or red emission, respectively. The morphology of the micro-/nanostructures is demonstrated to impact the device performance as well, as hollow architectures improve the photoluminescent/photocatalytic properties due to enhanced scattering and reflection of incident light, thereby increasing light harvesting efficiency.[40–43] With respect to energy applications, $ZnGa_2O_4$-based nanoparticles have also been characterized regarding their electrochemical performance for Li-ion batteries.[44,45] Using the here described networked material based on interconnected hollow metal oxide microstructures, an increase in the volumetric loading capacity of Li-ions and improvement of its cyclic stability by the reduction of diffusion pathways could potentially be facilitated.[8]

This work focuses on the investigation of the solid-state transformation reaction of aero-GaN(ZnO) networks into gallium oxide-based aero-Ga_2O_3/$ZnGa_2O_4$ networks and explores their photoluminescent and electrochemical performance. X-ray powder diffraction (XRPD) combined with Rietveld refinements, in situ XRPD heating experiments, and TEM investigations were carried out on selected samples of hybrid gallium oxide nanostructures composed of β-Ga_2O_3 and $ZnGa_2O_4$ phases. The growth of a $ZnGa_2O_4$ phase is a feature of the epitaxially and chemically stabilized thin layer of ZnO(-rich) phase on the interior wall of aero-GaN(ZnO) structures. The annealing experiments further demonstrate the possibility to tune the nanocrystalline structure by the choice of annealing temperature. Studies of the network's optical luminescence under UV light excitation demonstrate a transition from broadband visible light emission observed for aero-GaN(ZnO) toward narrow green emission bands centered around 504 nm for the hybrid aero-Ga_2O_3/$ZnGa_2O_4$ nanocomposite showing potential for application as high-temperature stable green phosphor. The electrochemical performance during cyclic voltammetry (CV) was tested and showed high initial capacities of ≈714 mAh g^{-1} at 100 mA g^{-1} and exceptional rate performance at high current densities of 4 A g^{-1} with 347 mAh g^{-1}, which is partially explained by the enhanced diffusion kinetics with highly accessible surface regions well connected in the 3D-structured network morphology with respect to nanoparticle agglomerates.

2. Results and Discussion

2.1. Materials Synthesis

The synthesis process of the gallium-oxide based β-Ga_2O_3/$ZnGa_2O_4$ aero-materials is schematically depicted in **Figure 1**. Initially, a light-weight, porous ZnO network (T-ZnO) containing interpenetrating solid micro-tetrapod and nanowire morphologies produced by a modified flame transport synthesis (FTS)[46] is shaped into a sample pellet (Figure 1a). These are sacrificial templates for the synthesis of aero-GaN(ZnO) networks by the hydride vapor phase epitaxy (HVPE) method as described in more detail in the Experimental Section. The resulting aero-GaN(ZnO) tetrapod structures (Figure 1b) feature thin walls t_{wall} < 25–50 nm of single crystalline GaN with a ZnO-(rich) ultrathin layer on the inner surface exhibiting outstanding chemical robustness against the high-temperature corrosive atmosphere by epitaxial stabilization.[23]

In this study, the aero-GaN(ZnO) networks are converted into hybrid aero-β-Ga_2O_3/$ZnGa_2O_4$ nanocomposites via an interfacial solid-state reaction by annealing under atmospheric conditions for about 60 min at T = 950 °C and T = 1100 °C (Figure 1c).[27,28]

2.2. X-Ray Diffraction Analyses and In Situ Observation

The XRPD pattern of the aero-GaN(ZnO) (see **Figure 2**a) shows that the dominant phase is GaN, shoulders of weak intensity

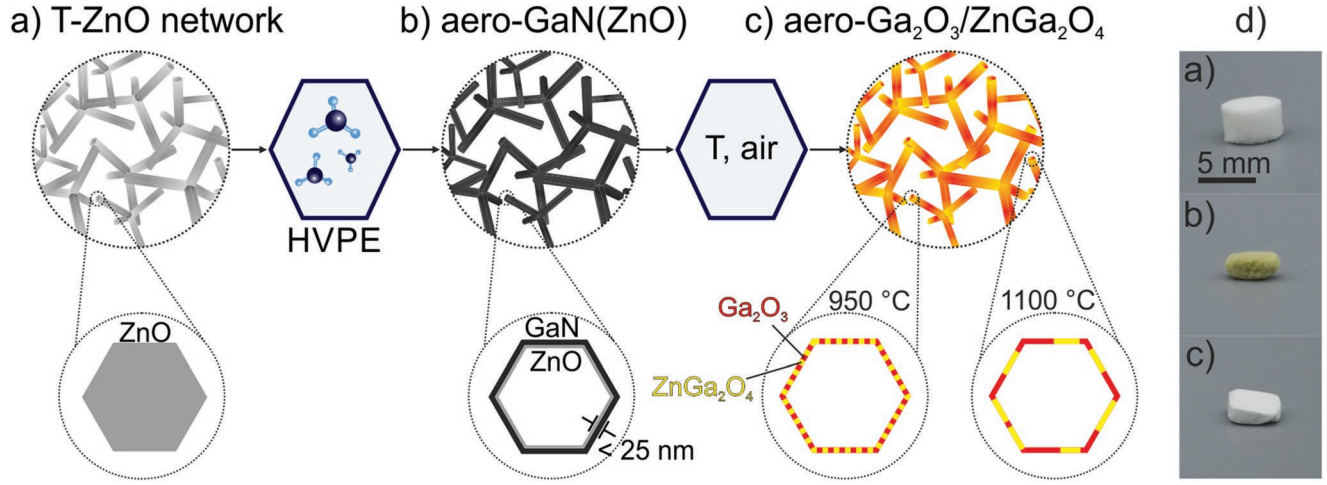

Figure 1. Sample photographs and schematic of the two-step synthesis process of gallium oxide-based aero-networks. a) Macroporous networks of interconnected ZnO tetrapods are used as sacrificial templates for the HVPE growth of b) aero-GaN(ZnO) networks which are transformed into hybrid nanocomposite structures of c) β-Ga_2O_3/$ZnGa_2O_4$ with annealing at 950 and 1100 °C. d) Photographs of the physical network structures.

may point to minor impurities but do not match GaN. This underlines the successful etching of the T-ZnO and shows that the remaining thin layer of ZnO must either be amorphous or it exists as heavily strained or mixed phase at the interface with GaN. A Pawley fit was used to further analyze the data. The lattice parameters (a = 3.20457(8) Å, c = 5.1925(2) Å) show a significant expansion compared to literature data for hexagonal GaN grown by different methods, where a varies between

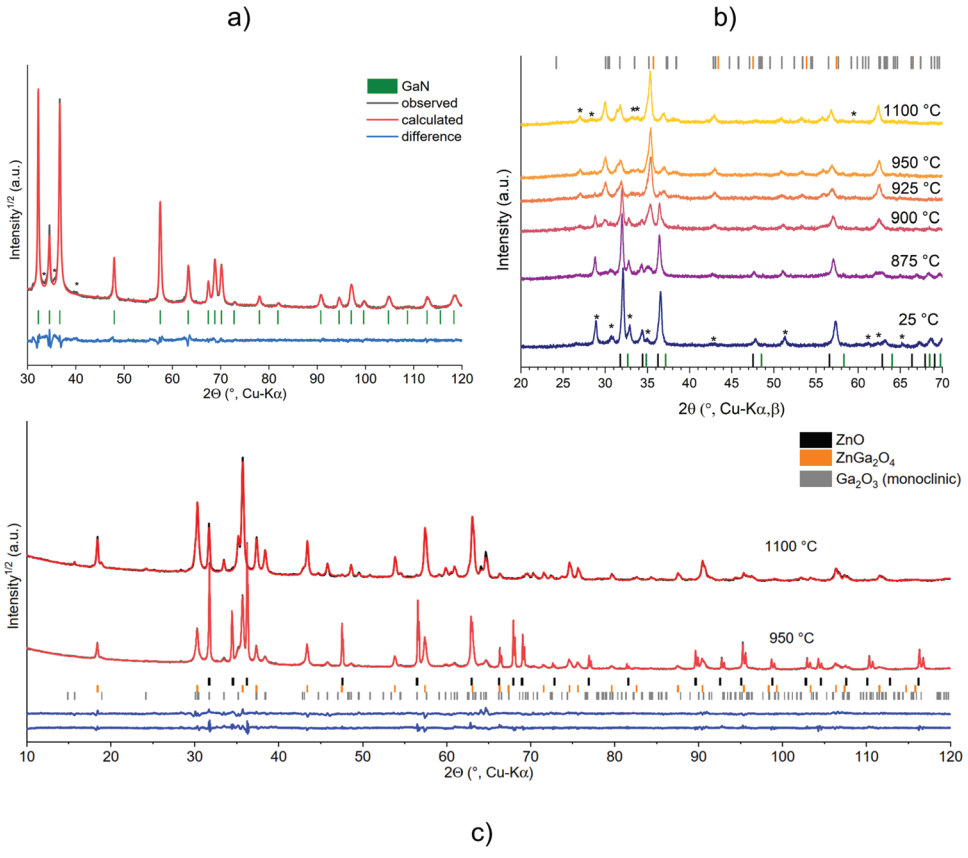

Figure 2. XRPD studies of the aero-GaN(ZnO) network material. a) Difference plot for the Pawley fit of the pristine aero-GaN(ZnO) network, r_{wp} = 4.9%, r_{exp} = 2.0%. The asterisks mark weak, unidentified reflections. b) In situ XRPD study of the transformation reaction. The asterisks mark satellite reflections due to the use of unfiltered radiation. The color of the tick marks coincides with those given in panels (a) and (c). Difference plots of the Rietveld refinements for the aero-Ga_2O_3/$ZnGa_2O_4$ composites annealed at 950 and 1100 °C. r_{wp} = 5.1/4.6%, r_{exp} = 1.8/2.0%, respectively.

3.1875 and 3.1893 Å and c = 5.1843–5.1867 Å.[47] Since the differences in lattice parameters between the literature data and the aero-GaN(ZnO) are much more pronounced for a, this points toward a sample related phenomenon rather than a systematic offset. The lattice parameters of wurtzite type ZnO are slightly larger (a = 3.2497 Å, c = 5.206 Å),[48] thus the expansion of the lattice parameters may be explained either by a strain effect due to epitaxial growth on the ZnO lattice and/or a partial mixing of the two phases at least at the interface.

The reflections of the GaN show significant and anisotropic line broadening which may originate from the crystallite size, strain, or combined effects. It turned out that both size and strain effects had to be considered for a convincing fit. Given the strong correlation among parameters for size and strain broadening the problem was simplified to an isotropic strain model and anisotropic size broadening. The volume weighted average domain size D_{Vol} from the $h00$ reflections is 89(6) nm, while the smallest value for D_{Vol} was found for $00l$ with 25(3) nm. It should be noted that using an anisotropic model for strain and isotropic size model yields virtually identical results in terms of the fit quality, but using the crystallite size appears reasonable given the finite thickness of the GaN walls.

The reaction from aero-GaN(ZnO) into hybrid nanocomposite aero-Ga_2O_3/$ZnGa_2O_4$ networks is investigated in detail by an in situ XRPD annealing experiment, the data is presented in Figure 2b. XRPD pattern were recorded up to a temperature of 1100 °C showing the transformation from the initial GaN(ZnO) phase to the gallium oxide nanocomposite between 850 and 950 °C. The majority of reflections are identified and indexed according to the cubic spinel-type structure of $ZnGa_2O_4$ (Fd-3m) and the monoclinic structure of β-Ga_2O_3 ($A2/m$) by comparison to references of crystallographic data.[49,50] Additional reflections which are inconsistent with these phases are marked with asterisks (*) and can be explained by the presence of K_β radiation for the in situ experiment (Figure 2c).

Two ex situ calcinated samples (950 and 1100 °C) were prepared for further studies, the XRPD patterns of which will be analyzed in greater detail (see Figure 2c) by means of Rietveld refinement for analyzing the quantitative composition and microstructure. They were prepared from different batches of the aero-GaN(ZnO) precursor, the one for the annealing at 950 °C contained reasonable amounts of T-ZnO remaining after the HVPE process which is also retained after calcination in air. Aside from that, both samples contain $ZnGa_2O_4$ and β-Ga_2O_3 as crystalline phases. The aero-Ga_2O_3/$ZnGa_2O_4$ annealed at 950 °C contains 47.0(1) wt% ZnO, 37.1(1) wt% of the spinel and 15.8(2) wt% Ga_2O_3. After annealing at 1100 °C 63.5(2) and 36.5(2) wt% are obtained for the latter two phases, which corresponds to 21.5 at% Zn, and no T-ZnO is observed. Thus, the ratio of $ZnGa_2O_4$ to Ga_2O_3 is similar, with the sample annealed at 950 °C containing more of the spinel, which is reasonable given the additional amount of ZnO that was available. The large amount of ZnO in the 950 °C sample further hints at the additional ZnO being not sufficiently close to the Ga_2O_3 (as for remaining T-ZnO), otherwise, a complete conversion to the spinel would be expected. For the $ZnGa_2O_4$ spinel, the crystallite size could be refined with D_{Vol} = 37.0(5) and 40.2(5) nm after annealing at 950 and 1100 °C, respectively, being in good agreement with the results from the TEM analysis (vide infra). For the monoclinic β-Ga_2O_3, modeling of the domain sizes was more complex: For the sample annealed at lower temperature, an isotropic domain size of 14(2) nm was derived, while after annealing at 1100 °C, an anisotropic model was advantageous with the r_{wp} dropping from 5.4 to 4.6%. Still for comparison, the isotropic size is reported with 32(1) nm, the anisotropic domain size ranges from 22(3) nm ($h00$ and $h0l$) to 60(3) nm ($00l$). This unexpected result is supported to some extent by the respective scanning transmission electron microscopy-energy dispersive X-ray spectroscopy (STEM-EDS) maps: If the agglomerations of Zn and Ga (see Figures 5 and 6) are assumed to stem from individual crystallites then the Ga_2O_3 particles do not show a defined morphology after annealing at 950 °C, while parts of the sample annealed at 1100 °C clearly show elongated morphologies.

2.3. Morphology of Aero-Network Microstructures

The morphologies of the pristine T-ZnO and aero-GaN(ZnO) networks and annealed aero-gallium oxide-based networks are displayed in the SEM images of **Figure 3**. The overview and magnified SEM micrographs of the aero-networks in general show hollow tubes with hexagonal motif predefined by the T-ZnO template.

Chemical analysis (cf. Table SI, Supporting Information) via EDS is conducted on all samples to follow the oxidation process of the GaN(ZnO) material. The EDS analysis reveals residual amounts of Zn, Zn/(Zn+Ga) of up to 22%, in the pristine aero-GaN(ZnO) network, which may originate from the ZnO(-rich) layer at the inner walls of the microtube structures. SEM micrographs of annealed network structures are shown in Figure 3b,c after treatment at 950 and 1100 °C, respectively. The micrographs display a modified surface structure of the tubes maintaining the hexagonal motif and a characteristic wall porosity, which is increasing in pore size with annealing temperature. Further, oblique views onto the cross-sections of the tubes allow to determine intergrown structures and reveal a larger wall thickness for the aero-Ga_2O_3/$ZnGa_2O_4$ (950 °C) sample compared to the pristine and aero-Ga_2O_3/$ZnGa_2O_4$ (1100 °C) sample. This observation could indicate inhomogeneities during the growth step of GaN or the choice of different process parameters, for example, growth time. As already discussed above, the sample annealed at 950 °C also stems from a different batch of the aero-GaN(ZnO) precursor than those samples presented in Figures 3a,c. In addition, XRPD analysis (cf. Figure 2c) demonstrated high amounts of ZnO originating from not fully reacted T-ZnO which is believed to survive the HVPE process in the center of the T-ZnO templates after high-temperature densification due to kinetic limitations. Therefore, the Zn/(Zn+Ga) ratio measured by EDS (see Table SI, Supporting Information) and determined by Rietveld analysis deviates from the phase pure precursor material and the calcinated (1100 °C) network. However, the EDS analysis performed on aero-Ga_2O_3/$ZnGa_2O_4$ network structures after annealing at 950 °C confirms the complete structural transformation showing no characteristic N(K) X-ray signal of GaN. Moreover, the average content of Zn associated with the phase pure aero-GaN(ZnO) microstructures and hybrid aero-Ga_2O_3/$ZnGa_2O_4$

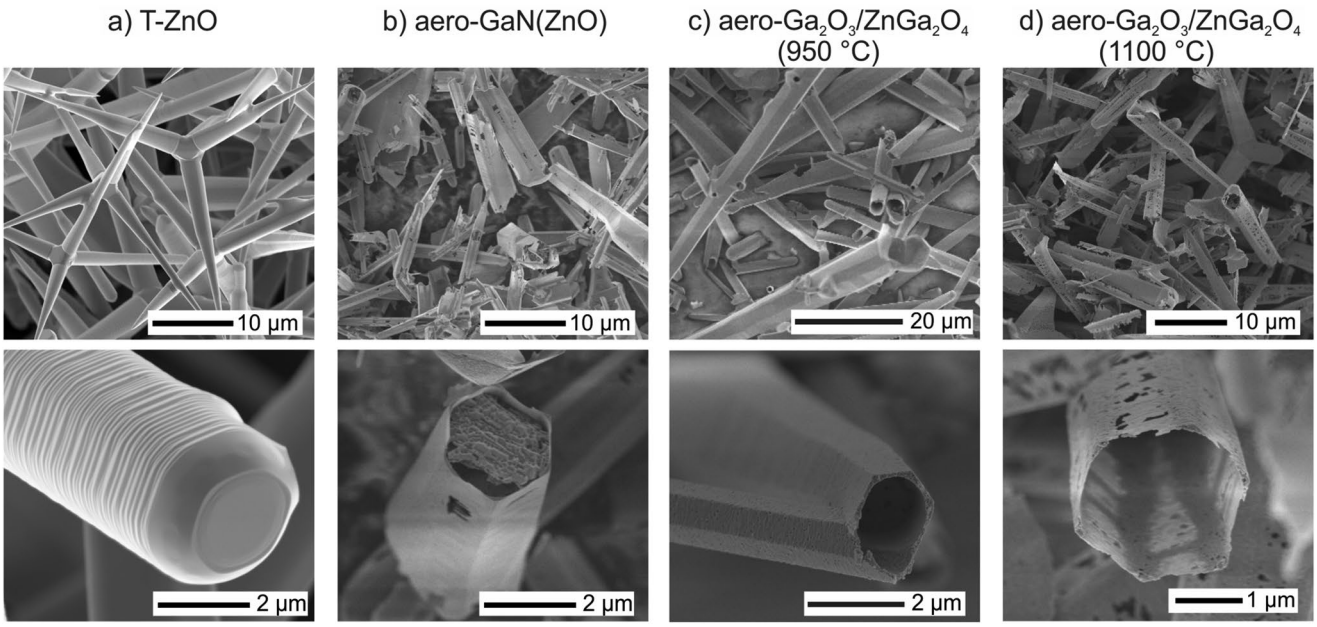

Figure 3. SEM micrographs of the a) T-ZnO template, the b) aero-GaN(ZnO) precursor, and aero-Ga_2O_3/$ZnGa_2O_4$ network structures after annealing at c) 950 °C and d) 1100°C.

nanocomposite structures after annealing to 1100 °C remains constant at a Zn/(Zn+Ga) ratio of ≈1/5, which is highly consistent with Rietveld quantification of ≈21.5 at% of Zn given above.

2.4. Nanostructure Analysis by TEM

After investigating the average structures of the pristine and annealed aero-materials by XRPD, the local structural peculiarities of the pristine aero-GaN(ZnO) and the annealed aero-gallium oxide networks were examined by TEM. The TEM investigations on the pristine aero-GaN(ZnO) network precursor structures are presented in **Figure 4** adding new EDS data to our previous examinations on these structures.[23,29] The end of a single hollow tube of GaN(ZnO) which is probed for EDS investigation is shown in the STEM image of Figure 4a. The hollow GaN(ZnO) structures are single crystalline with their *c*–axis matching the growth direction of the former T-ZnO arms which is demonstrated by the selected-area electron diffraction (SAED) pattern (see inset in Figure 4a) and the respective high-resolution TEM (HRTEM) micrograph shown in Figure 4b. The lattice fringes of the *c*–axis {0001} planes of GaN are resolved by HRTEM in the direction of the growth axis of the T-ZnO template. The Fast Fourier Transformation (FFT, inset Figure 4b) image and the SAED pattern show the intensity distribution of[11–20] zone-axis orientations referenced to the wurtzite-type structure ($P6_3mc$). Consistent with the XRPD measurements, the evaluation of the lattice parameters from both HRTEM and SAED analysis concludes a slightly larger lattice parameter $c \approx 5.22$ Å than that of relaxed GaN.[47] The local chemical analysis by STEM-EDS mapping of Zn and Ga elements recorded within the red framed region of Figure 4a is presented in Figure 4c. The displayed maps of Zn and Ga show a uniform distribution, suggesting that a thin ZnO(-rich) layer remains present at the interface to GaN, even in the high-temperature corrosive atmosphere during HVPE growth. Quantified compositions of the STEM-EDS maps are given in Table SII, Supporting Information. Next to the tetrapod structures, the aero-networks also contain nanowire structures of identical chemical composition as discussed in Figure S1, Supporting Information and the accompanying text.

In delineation of the XRPD experiments, the complete oxidation of the pristine network is expected after annealing at 950 °C resulting in the transformation into a hybrid β-Ga_2O_3/$ZnGa_2O_4$ nanocomposite. However, powder diffraction is not able to laterally resolve the local distribution of the gallium oxide phases within individual hollow structures of the network, their morphology, or their nanocrystalline orientation. To examine those local structural details of the hybrid aero-β-Ga_2O_3/$ZnGa_2O_4$ nanocomposites TEM and STEM-EDS investigations are performed on samples annealed at 950 and 1100 °C.

The TEM analysis on a single hybrid Ga_2O_3/$ZnGa_2O_4$ nanocomposite structure produced by annealing at 950 °C is summarized in **Figure 5** showing the end of a hollow tube in the TEM image of Figure 5a. As already indicated by the SEM images, the highly porous morphology of the tube's walls is demonstrated by the STEM image shown in Figure 5a with small domain sizes in the order of 10–30 nm. Electron diffraction experiments (cf. Figure 5b) performed on such hollow porous structures show single crystalline like patterns, which are derived from the[11–20] pattern of aero-GaN(ZnO). The superposition of at least two sets of reflection patterns is evidenced from neighboring spots of the high intensity 0–20(β-Ga_2O_3) and 440($ZnGa_2O_4$) reflections (see inset of Figure 5b). With the help of kinematic simulations, the present diffraction pattern is identified as superposition of multiple crystal orientations and phases. These are the [-101] | [201] crystal orientations for the

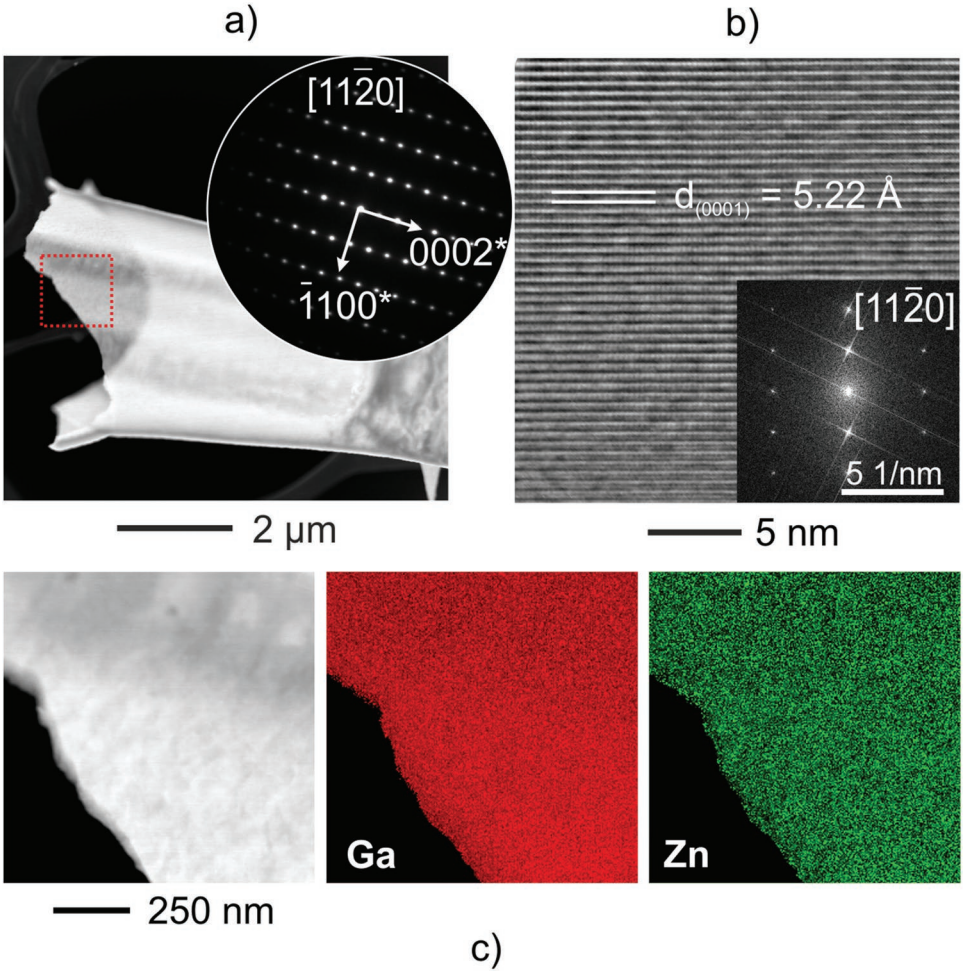

Figure 4. TEM analysis of aero-GaN(ZnO). a) STEM image showing an aero-GaN(ZnO) tetrapod arm. Inset: Electron diffraction pattern with single crystalline appearance in [11–20] zone axis orientation (wurtzite-type, $P6_3mc$). b) HRTEM micrograph and FFT (inset) showing the crystalline (0001) lattice fringes of GaN in [11–20] zone axis orientation. c) STEM-HAADF image of the red framed region depicted in (a) and the corresponding elemental distribution STEM-EDS maps Ga: red, Zn: green.

β-Ga_2O_3 phase and [112] for the $ZnGa_2O_4$ phase. Owing to only small differences in the interplanar spacings of spinel Fd-3m (111) of $ZnGa_2O_4$ and monoclinic $A2/m$ (202) and (10-2) of β-Ga_2O_3 lattice planes, structural compatibility is enabled perpendicular to the growth direction.[32] High-resolution imaging of the porous crystalline structure reveals single phase and hybrid phase regions, which describe the intergrowth of (11-1) planes of $ZnGa_2O_4$ with (202) planes of β-Ga_2O_3 as presented in Figure 5c. The transformation reaction from gallium nitride into gallium oxide species is facilitated via surface defects on the closed packed {0001} planes of the GaN epilayer acting as nucleation centers for the highly textured growth of crystalline Ga_2O_3.[51] Thereby, the single crystalline texture is preserved during the formation of the oxide phases along the closed packed {111} planes of the spinel-structure of $ZnGa_2O_4$ and the close lattice matching (202) or (10-2) planes of the monoclinic structure of β-Ga_2O_3. The early stage of this transformation reaction is investigated on aero-GaN(ZnO) tube structures after annealing at 750 °C (cf. Figure S2, Supporting Information). There, the experimental SAED patterns show diffuse streaks along 0001* in between the fundamental reflections. These developments of the diffraction patterns rationalize the solid-state reaction mechanism describing the formation of a hybrid nanocomposite. In close agreement with the structural examinations, STEM-EDS analysis (Figure 5d) conducted on the aero-Ga_2O_3/$ZnGa_2O_4$ structure in the red framed region of Figure 5a reveals the patterned distribution of the Ga_2O_3 and $ZnGa_2O_4$ phases and confirms the complete transformation from a nitride into an oxide microstructure after annealing at 950 °C. Quantified compositions of the STEM-EDS maps are given in Table SII, Supporting Information.

For direct comparison, aero-Ga_2O_3/$ZnGa_2O_4$ structures annealed at temperatures of 1100 °C during the in situ XRPD experiment are examined by TEM and STEM-EDS. Hereby, the influence of temperature on the evolution of the crystalline morphology is investigated and the results are summarized in **Figure 6**. Figure 6a displays two TEM images of tetrapod structures exhibiting a mixture of regions with high porosity and rather smooth surfaces, which exists as the majority morphology along the tetrapod facets (compare with Figure 6d,e).

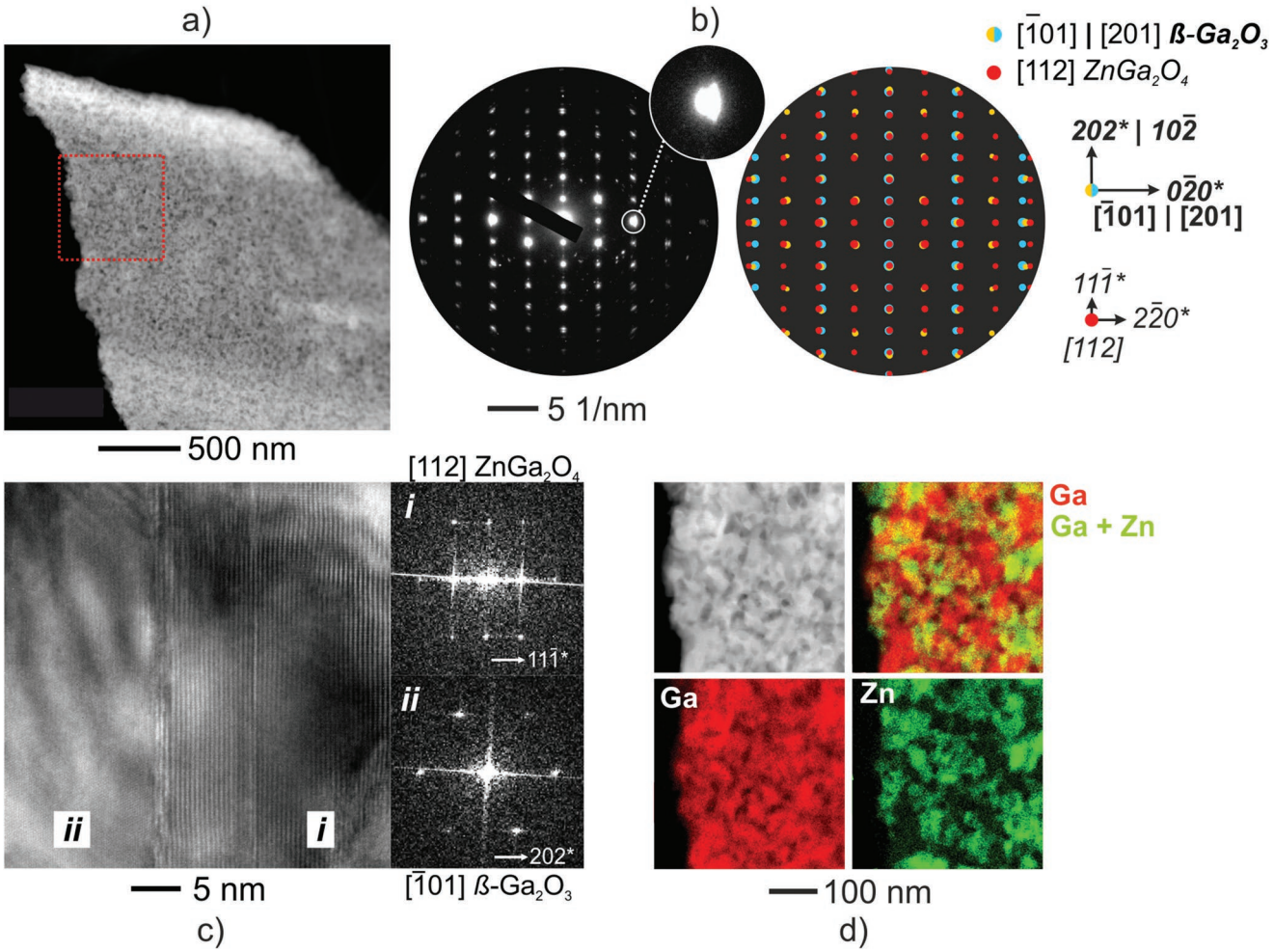

Figure 5. TEM analysis of aero-Ga_2O_3/$ZnGa_2O_4$ networks after annealing at 950 °C. a) STEM micrograph showing the porous morphology. b) Experimental electron diffraction pattern recorded on an aero-Ga_2O_3/$ZnGa_2O_4$ structure with split intensities (magnified inset). A superposition of kinematic ED simulations explains the experimental pattern by the superposition of two components β-Ga_2O_3 and $ZnGa_2O_4$ in [-101] and [112] orientations, respectively. c) HRTEM micrograph of a nanocrystal containing both binary and ternary oxide components. d) STEM-EDS elemental mapping from the red framed area in (a) showing the distribution of Ga: red and Zn: green, as well as their superposition to indicate binary and ternary phase oxides.

High-resolution microscopy from the smooth regions reveals relatively large crystal domains with high crystalline texture, for example, of the $ZnGa_2O_4$ phase, as depicted in Figure 6b. In addition, the effect of increased crystalline domains is reflected in SAED experiments, in comparison to patterns obtained on structures after annealing at 950 °C. The SAED pattern in Figure 6c shows the identical features of two superimposed components of a hybrid nanostructure as discussed before. However, the increased crystalline domain sizes (coherently scattering domains) of the two phases are reflected in smoothening of the diffraction spots. The change in crystalline morphology is followed by chemical analysis (cf. Figure 6d,e) recording STEM-EDS maps including both morphological constituents. In regions with high porosity the distribution of β-Ga_2O_3 and $ZnGa_2O_4$ phases is mapped showing undifferentiated distribution of grains with smaller domain sizes in the range of 50–100 nm, which is slightly larger but comparable to the sample annealed at 950 °C. However, in regions of the hexagonal facets, the crystal morphology exhibits lower porosity and larger and more differentiated domains of β-Ga_2O_3 and $ZnGa_2O_4$ with sizes larger than 200 nm. The separation into large single-phase domains can be explained by enhanced diffusion kinetics at higher temperatures and Ostwald ripening. Quantified compositions of the STEM-EDS maps are given in Table SII, Supporting Information. The 3D morphology of the hollow tubes is further imaged by volume reconstructions calculated from TEM tomography experiments. The representative images of a single hollow tube are presented in Figure 6f and demonstrate the sixfold symmetry of the tetrapod arm after annealing with smooth outer surfaces and more rough inner walls. Note, that the side facets are sometimes not correctly displayed due to their low thickness in comparison to the edges and not due to their structural absence.

In parallel to the described hollow tetrapod structures, nanowire structures composed of 50–100 nm large grains are observed to be composed of β-Ga_2O_3 and $ZnGa_2O_4$ as well and are described in more detail in the supporting text of Figure S3, Supporting Information.

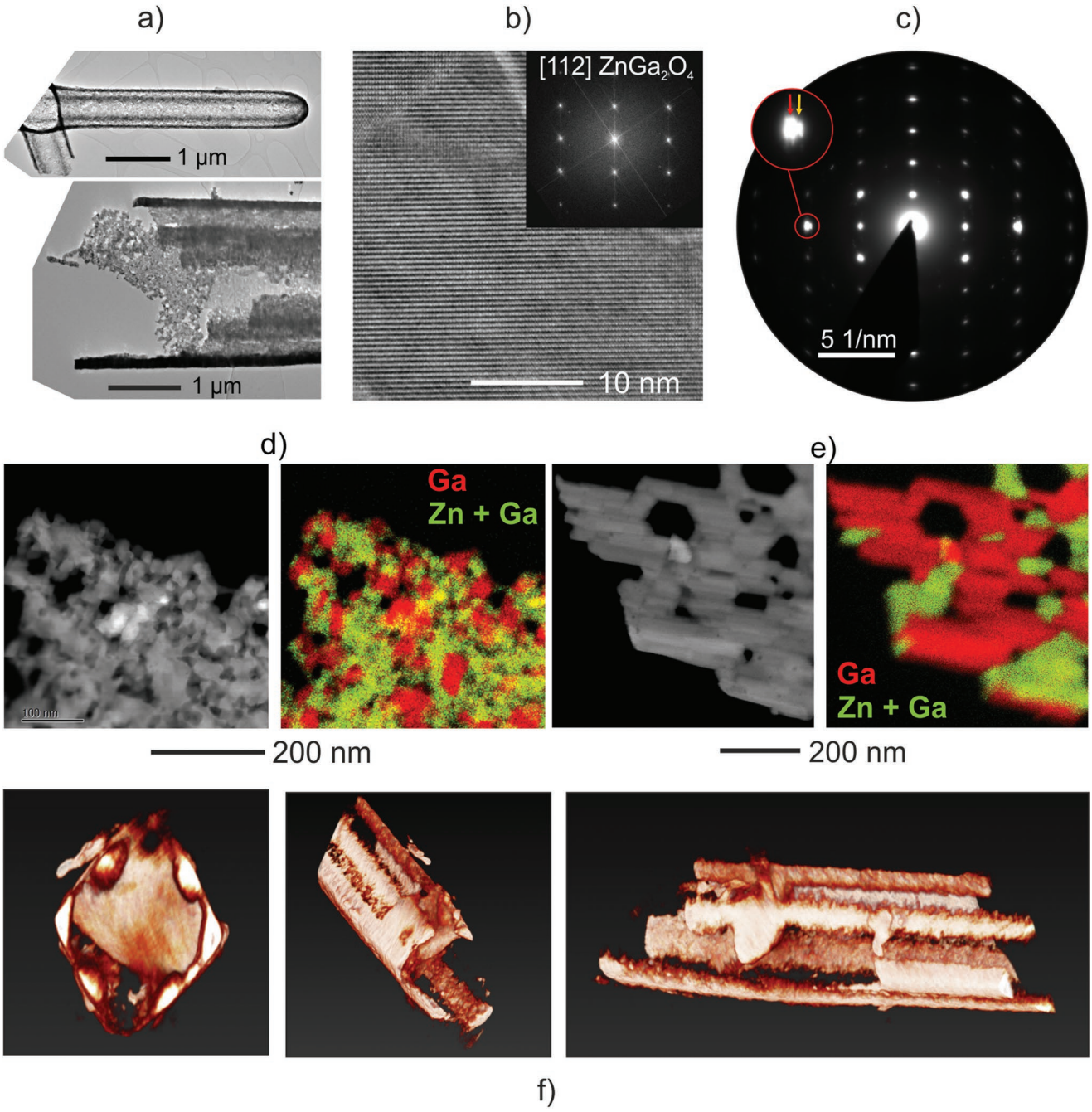

Figure 6. TEM analysis of aero-Ga_2O_3/$ZnGa_2O_4$ after annealing at 1100 °C. a) TEM images showing the arm of hollow $ZnGa_2O_4$ tubes composed of polycrystalline walls of different grain morphology. b) HRTEM micrograph and FFT image (inset) of a $ZnGa_2O_4$ crystal in [112] orientation. c) Electron diffraction pattern showing the [112] zone axis pattern of the $ZnGa_2O_4$ and the described [-101] and [201] patterns of β-Ga_2O_3. d) STEM-HAADF image showing a region with small grain structure and the corresponding EDS maps in overlay presentation depicting the distribution of β-Ga_2O_3 (red) and $ZnGa_2O_4$ (green) phase components. e) STEM-HAADF image showing a region with lamellar grain structure and the corresponding EDS maps in overlay presentation depicting the distribution of β-Ga_2O_3 (red) and $ZnGa_2O_4$ (green) phase components. f) Tomographic volume reconstructions of a hollow tube (without scale).

2.5. Photoluminescent Characterization

Further, the luminescent properties of the wide band-gap gallium-oxide based aero-networks were examined. For the analysis of optical properties, powders of the pristine aero-GaN(ZnO) networks and the hybrid nanocomposites of aero-Ga_2O_3/$ZnGa_2O_4$ annealed at temperatures of 950 and 1100 °C are examined. The emission spectra of aero-GaN(ZnO) (**Figure 7**a and Figure S3a, Supporting Information) show a broad emission band with a maximum in the visible light

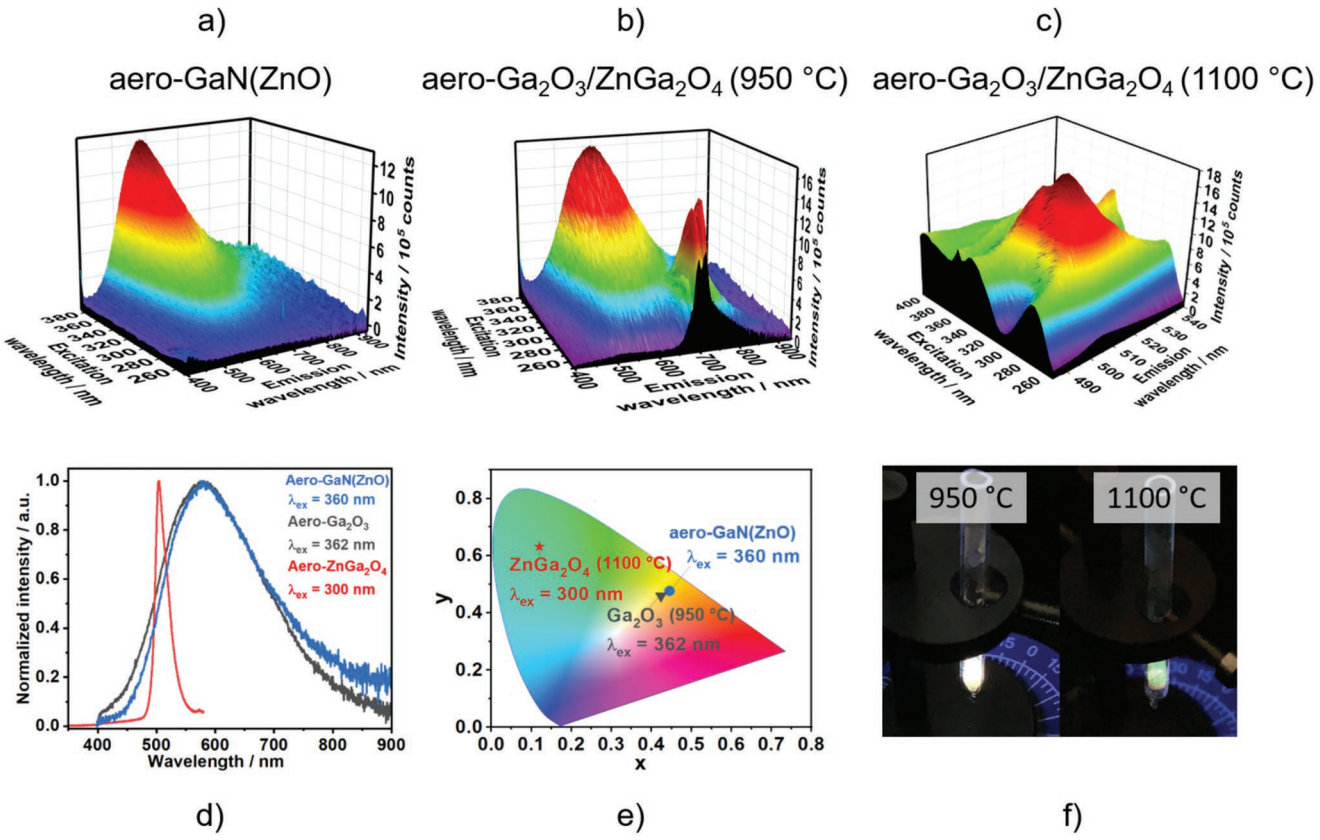

Figure 7. 3D emission and excitation spectra of a) aero-GaN(ZnO) and b) hybrid nanocomposite networks of aero-Ga_2O_3/$ZnGa_2O_4$ annealed at 950 °C and c) 1100 °C. d) Selected emission spectra of the aero-networks. e) CIE 1931 plot of color coordinates calculated from (d) and f) digital photographs of aero-Ga_2O_3/$ZnGa_2O_4$ networks annealed at 950 and 1100 °C under UV light excitation.

regime at 525 nm. The "yellow band" in GaN is commonly assigned to interband transistions, for example, discussed with C-doped lattice defects in GaN[52,53] or threading dislocations, for which the first seems plausible.[54] Further, the contribution of the ZnO(-rich) interface layer is plausible to add to the observed photoluminescence nonetheless its small volume fraction in the microstructures since there are strong similarities in band-edge and deep-center photoluminescence mechanisms of ZnO and GaN[55] which is apparent from reports of GaN[56–60] and ZnO in literature.[61,62]

The luminescence properties of the aero-materials are slightly shifted when converted from the aero-GaN(ZnO) to the hybrid aero-Ga_2O_3/$ZnGa_2O_4$ nanocomposite network structures. In the case of aero-Ga_2O_3/$ZnGa_2O_4$ annealed at 950 °C, upon excitation with high energies (e.g., λ_{ex} = 260 nm), a red-emitting doubled peak is observed at the range of 650–800 nm with maxima located at 695 and 711 nm, while excitation at a lower UV energy range (e.g., λ_{ex} = 360 nm) results in a very broad yellow emission band with maximum at 580 nm. This red-emitting double peak excitation spectrum also agrees with the phenomena often reported in literature, for instance, β-Ga_2O_3 nanostructures.[63–66] However, the origin of the yellow and the red bands still remains under intensive discussion. Here, the contribution of residual T-ZnO structures, which were identified by XRD on this sample, might as well superimpose the pure emission of nanocrystalline domains of Ga_2O_3 and $ZnGa_2O_4$ materials.

The optical properties of the aero-materials can be once more tuned by increasing the crystalline domain size of aero-Ga_2O_3/$ZnGa_2O_4$ with higher annealing temperature of 1100 °C. Hence, the structural changes result in the rise of a narrow emission band in the visible light region centered at 504 nm, previously attributed to the $^2E_A \rightarrow {}^4T_{2A}$ Ga^{3+} transition, which is related to delocalization of Ga^{3+} ions from octahedral into tetrahedral sites of the spinel structure.[67] The respective excitation spectrum consists of a broad band, mostly located at $\lambda <$ 350 nm, with maximum at 270 nm. The main emission spectra (Figure 7d, for more details, see Figure S4, Supporting Information) were used for calculating the color coordinates for aero-GaN(ZnO) ($x = 0.3160$, $y = 0.4799$), aero-Ga_2O_3/$ZnGa_2O_4$ (950 °C, abbreviated as aero-Ga_2O_3) (x = 0.4238, y = 0.4589) and aero-Ga_2O_3/$ZnGa_2O_4$ (1100 °C, abbreviated as aero- $ZnGa_2O_4$) (x = 0.1200, y = 0.6314), plotted in the Commission Internationale de l'éclairage (CIE) 1931 diagram in Figure 7e. In this context, it is important to notice that the most intense emission band of aero-GaN(ZnO) lies in the UV range and could therefore not be photographed for composing Figure 7f. In contrast, Figure 7f shows the yellow-white emission of aero-Ga_2O_3/$ZnGa_2O_4$ (950 °C) and the peaked green emission of aero-Ga_2O_3/$ZnGa_2O_4$ (1100 °C) under UV irradiation.

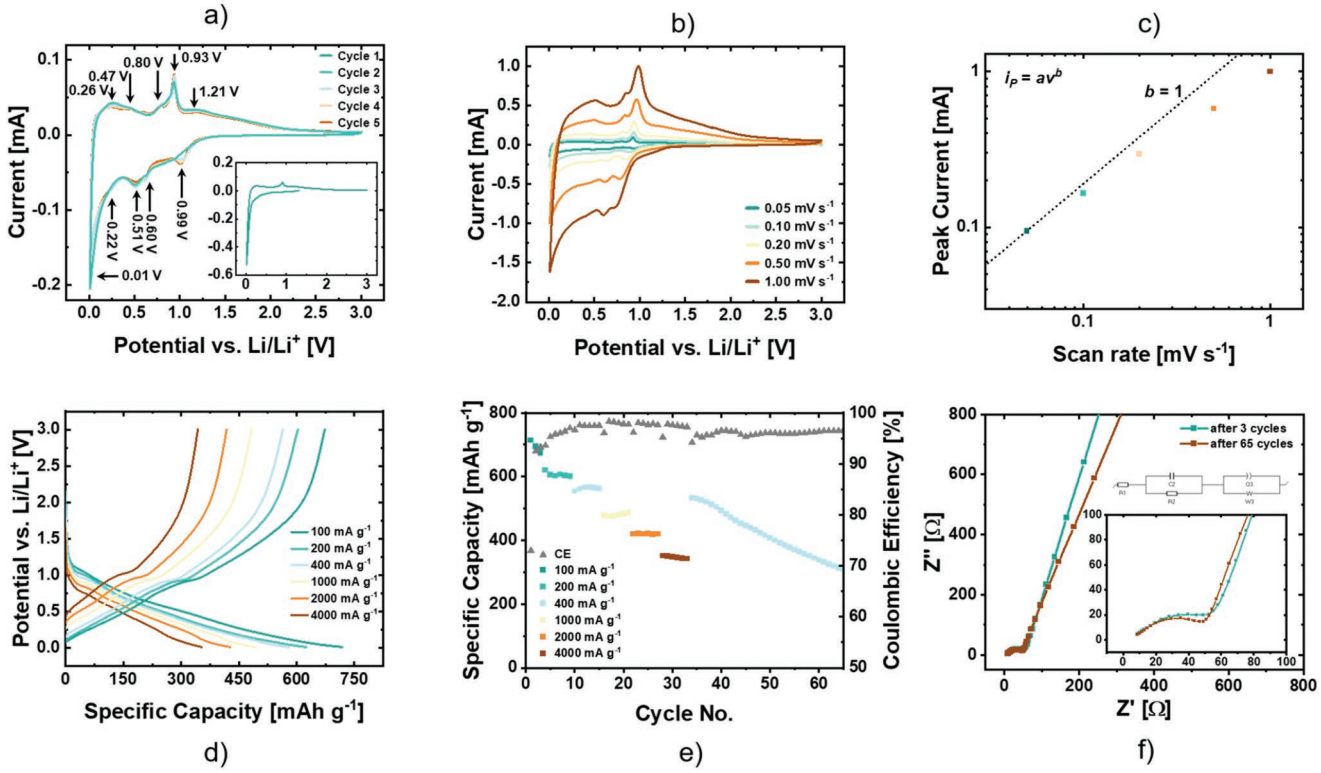

Figure 8. Electrochemical performance tests of the synthesized aero-Ga_2O_3/$ZnGa_2O_4$ (1100 °C) structures with (a) showing CV results from the first five cycles in between 0.01 and 3.0 V at a scan rate of 0.05 mV s^{-1} and b) a scan rate test ranging from 0.05 to 1 mV s^{-1}. (c) indicates the double logarithmic plot of the peak current for the oxidation peak against the scan rate with a dotted line representing a slope of 1. (d) shows galvanostatic charge and discharge curves under various current loads with e) the corresponding cycle dependency on the specific capacity. (f) shows electrochemical impedance spectroscopy cycles after the charging for cycles 3 and 65.

2.6. Electrochemical Characterization

Because of previous investigations of the electrochemical conversion reaction performance of $ZnGa_2O_4$ nanoparticles with Li-ions by Han et al.,[44,45] the synthesized network of aero-Ga_2O_3/$ZnGa_2O_4$ (1100 °C) was electrochemically characterized to investigate the influence of the special network morphology with high surface to volume ratio on the conversion kinetics and electrochemical capacitance. In this respect, **Figure 8**a shows the results from the CV measurement for the first five cycles at a scan rate of 0.05 mV s^{-1} for each cycle. The inset shows the first cycle, which differs strongly from the following cycles showing a strong reduction peak close to 0.01 V, which is indicating the decomposition of the initial Ga_2O_3 and $ZnGa_2O_4$ components and the conversion-type reactions into metallic Zn and Ga with the simultaneous formation of Li_2O according to:[45]

$$Ga_2O_3 + 6Li^+ + 6e^- \rightarrow 3Li_2O + 2Ga \quad (1)$$

$$ZnGa_2O_4 + 8Li^+ + 8e^- \rightarrow 4Li_2O + Zn + 2Ga \quad (2)$$

With the increasing number of cycles, numerous peaks are identified at 0.99, 0.60, 0.51, 0.22 V and 0.47, 0.8, 0.93, 1.21 V and attributed to the reduction and oxidation reactions during cyclic loading, respectively. The individual peaks could be related to various alloying mechanisms of Li_xZn ($x \leq 2$) and Li_yGa ($y \leq 2$) as reported elsewhere.[44,45] The exact elucidation of the reaction mechanism is beyond the scope of the present work. However, within the first five cycles the peak positions and peak heights stabilize showing decent cycling stability and reversible reactions.

Further, rate performance tests during CV (Figure 8c) elucidate the kinetics of the applied system. The peak current i_p during CV follows a power law dependence with respect to the applied scan rate v as follows:[68]

$$i_p(v) = av^b \quad (3)$$

with a and b being adjustable variables. For $b = 1$ the current contribution is mainly stemming from surface near activities, while for $b = 0.5$ the current is constrained by diffusion-controlled faradaic processes, mainly occurring inside the bulk side of the material. As shown in Figure 8b,c, the peak current determined for the oxidation-peak around 1 V exhibits a very responsive behavior with a nearly linear response of the current as the scan rate increases, with a value for b of around 0.82 for scan rates up to 0.2 mV s^{-1} indicating surface near reactions. This can be attributed to the thin layered morphology of the hollow tube-like structures with short diffusion pathways and a more capacitive-like behavior. With a higher scan rate, the b-value decreases continuously, so that the system becomes more and

more diffusion-controlled. However, even at 1 mV s^{-1}, narrow and sharp peaks are observed for oxidation and reduction processes, indicating a highly reversible reaction mechanism.

In addition, galvanostatic charge and discharge studies (Figure 8d,e) were performed to show the reversible capacity under various constant current loads. As can be seen, the voltage plateaus agree well with the peak values observed during CV (cf. Figure 8d,b). The initial reversible capacity was about 714 mAh g^{-1} at a current density of 100 mA g^{-1}, which agrees well with the theoretically achievable capacity of 819.6 mAh g^{-1} resulting from the initial composition of 63.5 wt% $ZnGa_2O_4$ and 36.5 wt% Ga_2O_3 (see discussion on Figure 2c), assuming the formation of Li_2O and metallic Zn and Ga. However, according to Han et al., alloy formation also occurs, indicating an even higher initial capacity.[44,45] Further studies are needed for detailed clarification. However, with increasing current density the capacity decreases to 606, 565, 465, 419, and 347 mAh g^{-1} for 200, 400, 1000, 2000, and 4000 mA g^{-1}, respectively. When returning to 100 mA g^{-1}, the capacity was still 532 mAh g^{-1}, indicating the physical integrity of the network structures even after cycling with high current rates. Thereafter, the reversible capacitance gradually decreased to 307 mAh g^{-1} within the next 33 cycles. In this aspect, related studies demonstrated the increase in cycle stability by embedding samples with reduced graphene oxide or N-doped carbon shells to prevent the Ga from aggregation during the cycling process and enhance electric conductivity.[69,70] SEM post-mortem analyses (see Figure S5, Supporting Information) still show hollow structures comparable to the initial tetrapodal shaped microstructures (cf. Figure 3) after 65 cycles, but indicate degradation of the material. This indicates that the aero-morphology remains stable over many cycles and that the decrease in capacity is most likely by a continuous electrical insulation of electrochemically active material due to the large volume changes.[71,72]

Electrochemical impedance studies (EIS) after the first three cycles and after cycling for 65 times are shown in Figure 8f. The overall behavior is similar to other structures based on $ZnGa_2O_4$ nanoparticle agglomerates.[44,45] The EIS data are fitted with the equivalent circuit model shown (see Figure 8f) and the results for the resistors are presented in **Table 1**.

Resistor R_1 can be related to the total series resistance of the cell including the housing, the separator, and both electrodes. Little change is observed here between the cycled sample, indicating that the overall integrity of the cell is maintained during cycling. The resistance R_2 can be related to the charge transfer resistances along the solid electrolyte interface and is of the same order of magnitude, decreasing only slightly after cycling.[44,45] This indicates the formation of a solid-electrolyte interface which is stable during cycling and acts as a well-functioning protective layer around the active battery components. The synthesized structures based on aero-Ga_2O_3/$ZnGa_2O_4$ (1100 °C) showed overall good electrochemical performance with high initial capacity of 714 mAh g^{-1} and good rate capability. Especially the latter showed a huge improvement in comparison to other $ZnGa_2O_4$-based anodes, which might be due to the well-controlled microstructure of the hybrid nanocomposite.

Table 1. Resistances obtained from an equivalent circuit model after 3 and 65 cycles.

	R_1 [Ohm]	R_2 [Ohm]
Cycle 3	5.472	57.49
Cycle 65	6.372	48.06

3. Summary and Conclusion

In this work, the temperature dependent growth and the crystalline nanostructure of an aero-Ga_2O_3/$ZnGa_2O_4$ network are thoroughly examined by in situ X-ray diffraction and TEM investigations. In a two-step synthesis process, aero-GaN(ZnO) networks were annealed in air atmosphere at 950 and 1100 °C yielding structurally intact hollow micro-tetrapods. The structural transformation of the nitride structure into gallium oxides by oxidation was observed in the narrow temperature interval of 850–950 °C. The resulting aero-gallium oxide networks contain polycrystalline hollow tetrapod and nanowire structures. In-depth structural characterization of these network structures produced by annealing at 950 and 1100 °C demonstrated a roughly 1:2 ratio of Ga_2O_3/$ZnGa_2O_4$ phase components and the tunability of the crystalline domain dimensions with temperature. The designed aero-Ga_2O_3/$ZnGa_2O_4$ networks are composed of intact hollow nanocrystalline tetrapod and nanowire morphologies with high chemical and temperature stability. The nanocomposite chemistry paired with the high surface to volume ratio (active area) and the 3D porous network character proved visible light excitation stimulated by UV-light irradiation and showed a transition from a broad band yellow emission into a narrow green-light emission band centered at 504 nm in agreement with the discussed structural changes. Studies of the electrochemical conversion performance in delineation of the 3D and porous character of the hybrid nanocomposites' hollow microstructures proved electrochemical activity with high initial capacities of 714 mAh g^{-1} and exceptionally good performance at high current load of up to 4 A g^{-1}, but fast fading capacity. This behavior can be mainly attributed to the thoroughly ordered microstructure of the hybrid composited with easily accessible surface regions of $ZnGa_2O_4$ and Ga_2O_3 for the electrochemical reactions and the formation of a solid-electrolyte interface, which would require further optimization for real electrochemical application, for example, the incorporation with reduced graphene oxide, improvement of the electrolyte with additives or the use of binders to increase thermal stability. The hybrid nanocomposite network material could also be an interesting candidate for the analysis of photocatalytic or gas sensing applications. The hybrid nanocomposite network material could also be an interesting candidate for the analysis of photocatalytic or gas sensing applications. Further, the diversity of the reported approach using sacrificial T-ZnO network templates promises analogous synthesis strategies of hybrid hierarchical structures containing zinc spinel oxides for diverse functionalities.

4. Experimental Section

Materials Synthesis: The synthesis of the presented aero-β-Ga_2O_3/$ZnGa_2O_4$ nanocomposite networks was based on the special hybrid chemical structure of the aero-GaN(ZnO) precursor material, in

which a ZnO(-rich) interfacial layer at the inner wall of the hollow tube structures was believed to be epitaxially intergrown to the outer GaN layer. The growth of such aero-GaN(ZnO) precursor structures was initiated by the HVPE method.[23] In detail, pressed pellets of the T-ZnO networks were placed in a four-temperature-zone-heated horizontal reactor, and together with metallic gallium (Ga), ammonia gas (NH_3), and hydrogen chloride (HCl) they were used as source materials for GaN growth. During the growth reaction, a hydrogen carrier gas transports the initial product GaCl from the source zone (T = 850 °C) into the reaction zone, where its reaction with NH_3 molecules (600 °C, 10 min) initiates the formation of an epitaxially grown single crystalline GaN layer onto the ZnO structures. During this growth step, the flow rates of HCl, NH_3, and H_2 were kept constant at 15, 500, and 3600 sml min^{-1}, respectively. Simultaneously, during the second step of the GaN growth process (850 °C, 10 min) the ZnO template structures were decomposed in the high-temperature corrosive atmosphere. Next, the obtained-aero-GaN(ZnO) networks were calcinated in air at 950 and 1100 °C for 1 h to result in the aero-β-Ga_2O_3/$ZnGa_2O_4$ nanocomposite networks.

Materials Characterization: The ratio of β-Ga_2O_3 to $ZnGa_2O_4$ oxide phases was further analyzed by a Rietveld analysis for the respective networks and the nanostructure morphology was examined in dependence of the annealing temperature by TEM as described in the following.

The pellets of the aero-GaN(ZnO) structures were used for temperature dependent examination of the reaction from the nitride to the oxide phase after 60 min of annealing at 950 and 1100 °C. XRPD was carried out on a Panalytical Empyrean diffractometer equipped with Ni filtered Cu-Kα radiation, soller slits (0.04 rad), a fixed divergence slit (0.25°), and a PIXcel 1D detector in Bragg-Brentano geometry. The samples were placed on low background sample holders made from Si. For the Rietveld refinements[73] TOPAS Academic version 6.0 was used.[74]Instrumental line broadening was described using the fundamental parameter approach as implemented in TOPAS and verified against a measurement of LaB_6 (NIST SRM 660c).[75] Where necessary, corrections for effects due to preferred orientation were made using the March-Dollase function for one direction as implemented in TOPAS. The transformation reaction into gallium oxide phases was further examined in situ by progressively annealing the network samples up to a maximum temperature of 1100 °C while performing θ–2θ scans at selected temperatures. Therefore, a Rigaku SmartLab (Cu(K) radiation (λ = 154 pm), 9 kW, Hypix detector) diffractometer was equipped with a graphite dome-shaped heating stage (AntonPaar, DHS 1100 Domed Hot Stage) with a maximum temperature deviation of ±2 °C for less than 1 mm thick samples. For the in situ annealing experiment, an interval of 25 °C was selected within a critical temperature range of 850–950 °C.

The microstructure morphology and chemical composition of the aero-networks before and after annealing were examined on a Zeiss Gemini ultra55 Plus field-emission scanning electron microscope equipped with an in-lens electron detector and a Silicon drift detector (Oxford Instruments) for EDS measurements. TEM analysis of the network structures was performed before and at selected steps of the oxidation reaction. The crystalline components of the hybrid nanocomposites were investigated by SAED experiments, HRTEM, and STEM combined with nanoscale chemical composition analysis via EDS. The studies were performed on multiple microscopes; a JEOL JEM-2100 (thermionic source LaB_6, 200 kV) instrument, a JEOL JEM-ARM200F "NEOARM" operated with a coldFEG (field emission gun) at 200 kV, and dual silicon drift detectors with each 100 mm^2 for EDS analysis and a TFS Tecnai F30 G^2 STwin (FEG, 300 kV) microscope.

The morphology of the hollow structures was modeled in 3D by bright field TEM electron tomography. Therefore, a saxton tilt series ranging from −54 to +54 degree with a maximum tilt step of 2° was performed on the JEM-ARM200F instrument. The recorded data was reconstructed using the simultaneous iterative reconstruction technique (20 iterations, multiplicative improve mode). For recording, reconstruction, and visualization of the respective parts, the TEMography software (System in Frontier Inc.) was used.

Luminescence Properties: Luminescence measurements were performed using a Fluorolog-3 fluorescence spectrometer FL322 (HORIBA Jovin Yvon GmbH, Unterhaching, Germany), equipped with a 450 W Xenon lamp, an iHR-320-FA triple grating imaging spectrograph, combined with a Syncerity CCD, and a R928P photomultiplier-based detector.

Electrochemical Properties: For the electrochemical characterization of the synthesized aero-Ga_2O_3/$ZnGa_2O_4$ (1100 °C) as electrode material, two electrode tests in half-cell configuration were performed using CR2032 coin cells. For this purpose, the aero-Ga_2O_3/$ZnGa_2O_4$ (1100 °C) network as active material was thoroughly mixed with carbon black (Super P) and CMC binder (Sigma Aldrich) in the ratio of 70:20:10 in a water-solvent dispersant. The resulting mixture was cast onto a Cu foil (thickness 50 µm) using a doctor blade approach and dried in a vacuum drying oven at 60 °C for 24 h. The active material loading of the coated Cu foil was determined gravimetrically using a microbalance and was around 1 mg cm^{-2}. The resulting aero-Ga_2O_3/$ZnGa_2O_4$ (1100 °C) working electrode was mounted in a CR2032 coin cell (MTI) with 100 µL of LP30 electrolyte (Sigma Aldrich), Li metal (Sigma Aldrich) as a counter electrode and a Whatmann separator (AH-934). LP30 was a commonly used carbonate electrolyte (EC/DMC, 1/1) with 1 M LiPF6. CV and galvanostatic (GCPL) tests were performed on a Biologic BCS805 system in a range of 0.01–3.0 V at room temperature. The scan rate and current density applied to the cell range from 0.05 to 1 mV s^{-1} and 100–4000 mA g^{-1}, respectively. EIS were measured using the same system over a frequency range of 10 mHz–10 kHz with an AC amplitude of 10 mV.

Supporting Information

Supporting Information is available from the Wiley Online Library or from the author.

Acknowledgements

The authors acknowledge funding from the Deutsche Forschungsgemeinschaft (DFG) under the scheme of the collaborative research center CRC 1261/A6. This work was carried out in the framework of the project "SuSiBaBy"—SulfurSilicon Batteries funded by the EUSH. Financial support by the federal state of Schleswig-Holstein is gratefully acknowledged (LPW-E/1.1.2/1486). This research was partially funded by the National Agency for Research and Development of the Republic of Moldova under the grant no. 20.80009.5007.20.

Open access funding enabled and organized by Projekt DEAL.

Conflict of Interest

The authors declare no conflict of interest.

Data Availability Statement

The data that support the findings of this study are available from the corresponding author upon reasonable request.

Keywords

cyclovoltammetry, gallium oxide, nanocomposite, network materials, structure analysis

Received: December 1, 2022
Revised: January 20, 2023
Published online: February 13, 2023

[1] X. W. (David) Lou, L. A. Archer, Z. Yang, *Adv. Mater.* **2008**, *20*, 3987.
[2] A.-H. Lu, F. Schüth, *Adv. Mater.* **2006**, *18*, 1793.
[3] F. Schüth, *Angew. Chem.* **2003**, *115*, 3730.
[4] L. Yu, X. Y. Yu, X. W. (David) Lou, *Adv. Mater.* **2018**, *30*, 1800939.
[5] L. Yu, H. Hu, H. B. Wu, X. W. (David) Lou, *Adv. Mater.* **2017**, *29*, 1604563.
[6] Y. Huang, X. Hu, J. Li, J. Zhang, D. Cai, B. Sa, H. Zhan, Z. Wen, *Energy Storage Mater.* **2020**, *29*, 121.
[7] F. Ma, J. Lu, L. Pu, W. Wang, Y. Dai, *J. Colloid Interface Sci.* **2020**, *563*, 435.
[8] Z. Wang, L. Zhou, X. W. (David) Lou, *Adv. Mater.* **2012**, *24*, 1903.
[9] W. Wei, Z. Wang, Z. Liu, Y. Liu, L. He, D. Chen, A. Umar, L. Guo, J. Li, *J. Power Sources* **2013**, *238*, 376.
[10] K. Huang, Y. Sun, Y. Zhang, X. Wang, W. Zhang, S. Feng, *Adv. Mater.* **2019**, *31*, 1801430.
[11] M. Xiao, Z. Wang, M. Lyu, B. Luo, S. Wang, G. Liu, H.-M. Cheng, L. Wang, *Adv. Mater.* **2019**, *31*, 1801369.
[12] J.-H. Lee, *Sens. Actuators, B* **2009**, *140*, 319.
[13] Y. Liu, S. Xiao, K. Du, *Adv. Mater. Interfaces* **2021**, *8*, 2002122.
[14] R. Wei, Y. Xu, M. Xue, *J. Mater. Chem. B* **2021**, *9*, 1965.
[15] Y. He, W. Chen, X. Li, Z. Zhang, J. Fu, C. Zhao, E. Xie, *ACS Nano* **2013**, *7*, 174.
[16] C. Li, Z. Li, X. Qi, X. Gong, Y. Chen, Q. Peng, C. Deng, T. Jing, W. Zhong, *J. Colloid Interface Sci.* **2022**, *605*, 13.
[17] H. Luo, D. Ji, Z. Yang, Y. Huang, G. Xiong, Y. Zhu, R. Guo, Y. Wan, *Chem. Eng. J.* **2017**, *326*, 151.
[18] F. Schütt, F. Rasch, N. Deka, A. Reimers, L. M. Saure, S. Kaps, J. Rank, J. Carstensen, Y. Kumar Mishra, D. Misseroni, A. Romani Vázquez, M. R. Lohe, A. Shaygan Nia, N. M. Pugno, X. Feng, R. Adelung, *Mater. Today* **2021**, *48*, 7.
[19] Y.-G. Zhang, Y.-J. Zhu, F. Chen, T.-W. Sun, *ACS Appl. Mater. Interfaces* **2017**, *9*, 7918.
[20] M. Mecklenburg, A. Schuchardt, Y. K. Mishra, S. Kaps, R. Adelung, A. Lotnyk, L. Kienle, K. Schulte, *Adv. Mater.* **2012**, *24*, 3486.
[21] F. Rasch, F. Schütt, L. M. Saure, S. Kaps, J. Strobel, O. Polonskyi, A. S. Nia, M. R. Lohe, Y. K. Mishra, F. Faupel, L. Kienle, X. Feng, R. Adelung, *ACS Appl. Mater. Interfaces* **2019**, *11*, 44652.
[22] T. Braniste, S. Zhukov, M. Dragoman, L. Alyabyeva, V. Ciobanu, M. Aldrigo, D. Dragoman, S. Iordanescu, S. Shree, S. Raevschi, R. Adelung, B. Gorshunov, I. Tiginyanu, *Semicond. Sci. Technol.* **2019**, *34*, 12LT02.
[23] I. Tiginyanu, T. Braniste, D. Smazna, M. Deng, F. Schütt, A. Schuchardt, M. A. Stevens-Kalceff, S. Raevschi, U. Schürmann, L. Kienle, N. M. Pugno, Y. K. Mishra, R. Adelung, *Nano Energy* **2019**, *56*, 759.
[24] F. Schütt, M. Zapf, S. Signetti, J. Strobel, H. Krüger, R. Röder, J. Carstensen, N. Wolff, J. Marx, T. Carey, M. Schweichel, M.-I. Terasa, L. Siebert, H.-K. Hong, S. Kaps, B. Fiedler, Y. K. Mishra, Z. Lee, N. M. Pugno, L. Kienle, A. C. Ferrari, F. Torrisi, C. Ronning, R. Adelung, *Nat. Commun.* **2020**, *11*, 1437.
[25] I. Hölken, G. Neubüser, V. Postica, L. Bumke, O. Lupan, M. Baum, Y. K. Mishra, L. Kienle, R. Adelung, *ACS Appl. Mater. Interfaces* **2016**, *8*, 20491.
[26] I. Plesco, T. Braniste, N. Wolff, L. Gorceac, V. Duppel, B. Cinic, Y. K. Mishra, A. Sarua, R. Adelung, L. Kienle, I. Tiginyanu, *APL Mater.* **2020**, *8*, 061105.
[27] T. Braniste, M. Dragoman, S. Zhukov, M. Aldrigo, V. Ciobanu, S. Iordanescu, L. Alyabyeva, F. Fumagalli, G. Ceccone, S. Raevschi, F. Schütt, R. Adelung, P. Colpo, B. Gorshunov, I. Tiginyanu, *Nanomaterials* **2020**, *10*, 1047.
[28] I. Plesco, V. Ciobanu, T. Braniste, V. Ursaki, F. Rasch, A. Sarua, S. Raevschi, R. Adelung, J. Dutta, I. Tiginyanu, *Materials* **2021**, *14*, 1985.
[29] N. Wolff, V. Ciobanu, M. Enachi, M. Kamp, T. Braniste, V. Duppel, S. Shree, S. Raevschi, M. Medina-Sánchez, R. Adelung, O. G. Schmidt, L. Kienle, I. Tiginyanu, *Small* **2020**, *16*, 1905141.
[30] O. Parlak, Y. Kumar Mishra, A. Grigoriev, M. Mecklenburg, W. Luo, S. Keene, A. Salleo, K. Schulte, R. Ahuja, R. Adelung, A. P. F. Turner, A. Tiwari, *Nano Energy* **2017**, *34*, 570.
[31] Z. Galazka, S. Ganschow, R. Schewski, K. Irmscher, D. Klimm, A. Kwasniewski, M. Pietsch, A. Fiedler, I. Schulze-Jonack, M. Albrecht, T. Schröder, M. Bickermann, *APL Mater.* **2019**, *7*, 022512.
[32] R.-H. Horng, C.-Y. Huang, S.-L. Ou, T.-K. Juang, P.-L. Liu, *Cryst. Growth Des.* **2017**, *17*, 6071.
[33] T. Omata, N. Ueda, K. Ueda, H. Kawazoe, *Appl. Phys. Lett.* **1994**, *64*, 1077.
[34] Z. Wang, K. Teramura, S. Hosokawa, T. Tanaka, *J. Mater. Chem. A* **2015**, *3*, 11313.
[35] M.-R. Wu, W.-Z. Li, C.-Y. Tung, C.-Y. Huang, Y.-H. Chiang, P.-L. Liu, R.-H. Horng, *Sci. Rep.* **2019**, *9*, 7459.
[36] X. Zhang, J. Huang, K. Ding, Y. Hou, X. Wang, X. Fu, *Environ. Sci. Technol.* **2009**, *43*, 5947.
[37] M.-I. Chen, A. K. Singh, J.-L. Chiang, R.-H. Horng, D.-S. Wuu, *Nanomaterials* **2020**, *10*, 2208.
[38] H.-J. Byun, J.-U. Kim, H. Yang, *Nanotechnology* **2009**, *20*, 495602.
[39] Z. Gu, F. Liu, X. Li, J. Howe, J. Xu, Y. Zhao, Z. Pan, *J. Phys. Chem. Lett.* **2010**, *1*, 354.
[40] Y. Hao, J. Zhang, M. Bi, Z. Feng, K. Bi, *Mater. Des.* **2018**, *155*, 257.
[41] H. Li, Z. Bian, J. Zhu, D. Zhang, G. Li, Y. Huo, H. Li, Y. Lu, *J. Am. Chem. Soc.* **2007**, *129*, 8406.
[42] G. Murali, S. Kaur, Y. C. Chae, M. Ramesh, J. Kim, Y. D. Suh, D.-K. Lim, S. H. Lee, *RSC Adv.* **2017**, *7*, 24255.
[43] L. Zong, Z. Wang, R. Yu, *Small* **2019**, *15*, e1804510.
[44] N. Han, Y. Xia, Y. Han, X. Jiao, D. Chen, *Appl. Surf. Sci.* **2018**, *433*, 983.
[45] N. Han, D. Chen, Y. Pang, Z. Han, Y. Xia, X. Jiao, *Electrochim. Acta* **2017**, *235*, 295.
[46] Y. K. Mishra, S. Kaps, A. Schuchardt, I. Paulowicz, X. Jin, D. Gedamu, S. Freitag, M. Claus, S. Wille, A. Kovalev, S. N. Gorb, R. Adelung, *Part. Part. Syst. Charact.* **2013**, *30*, 775.
[47] V. Darakchieva, B. Monemar, A. Usui, *Appl. Phys. Lett.* **2007**, *91*, 031911.
[48] R. R. Reeber, *J. Appl. Phys.* **1970**, *41*, 5063.
[49] J. Åhman, G. Svensson, J. Albertsson, *Acta Crystallogr., Sect. C: Struct. Chem.* **1996**, *52*, 1336.
[50] M. Allix, S. Chenu, E. Véron, T. Poumeyrol, E. A. Kouadri-Boudjelthia, S. Alahraché, F. Porcher, D. Massiot, F. Fayon, *Chem. Mater.* **2013**, *25*, 1600.
[51] T. Yamada, J. Ito, R. Asahara, K. Watanabe, M. Nozaki, S. Nakazawa, Y. Anda, M. Ishida, T. Ueda, A. Yoshigoe, T. Hosoi, T. Shimura, H. Watanabe, *J. Appl. Phys.* **2017**, *121*, 035303.
[52] T. Ogino, M. Aoki, *Jpn. J. Appl. Phys.* **1980**, *19*, 2395.
[53] R. Zhang, T. F. Kuech, *Appl. Phys. Lett.* **1998**, *72*, 1611.
[54] B. Liu, F. Yuan, B. Dierre, T. Sekiguchi, S. Zhang, Y. Xu, X. Jiang, *ACS Appl. Mater. Interfaces* **2014**, *6*, 14159.
[55] D. C. Reynolds, D. C. Look, B. Jogai, H. Morkoç, *Solid State Commun.* **1997**, *101*, 643.
[56] M. Kumar, S. K. Pasha, T. C. S. Krishna, A. P. Singh, P. Kumar, B. K. Gupta, G. Gupta, *Dalton Trans.* **2014**, *43*, 11855.
[57] B. Kuppulingam, K. Baskar, *Emergent Mater.* **2020**, *3*, 591.
[58] M. Matys, B. Adamowicz, *J. Appl. Phys.* **2017**, *121*, 065104.
[59] G. Nabi, C. Cao, S. Hussain, W. S. Khan, R. R. Sagar, Z. Ali, F. K. Butt, Z. Usman, D. Yu, *CrystEngComm* **2012**, *14*, 8492.
[60] A. G. Reddy, N. Aggarwal, T. C. Shibin Krishna, M. Singh, R. Rakshit, G. Gupta, *Appl. Phys. Lett.* **2015**, *106*, 233501.
[61] H. W. Kim, S. H. Shim, C. Lee, *Mater. Sci. Forum* **2006**, *518*, 137.
[62] J. H. Kim, E.-M. Kim, D. Andeen, D. Thomson, S. P. DenBaars, F. F. Lange, *Adv. Funct. Mater.* **2007**, *17*, 463.
[63] S. Kumar, G. Sarau, C. Tessarek, M. Y. Bashouti, A. Hähnel, S. Christiansen, R. Singh, *J. Phys. D: Appl. Phys.* **2014**, *47*, 435101.

[64] G. Naresh-Kumar, H. MacIntyre, S. Subashchandran, P. R. Edwards, R. W. Martin, K. Daivasigamani, K. Sasaki, A. Kuramata, *Phys. Status Solidi B* **2021**, *258*, 2000465.
[65] S. C. Vanithakumari, K. K. Nanda, *Adv. Mater.* **2009**, *21*, 3581.
[66] X. T. Zhou, F. Heigl, J. Y. P. Ko, M. W. Murphy, J. G. Zhou, T. Regier, R. I. R. Blyth, T. K. Sham, *Phys. Rev. B* **2007**, *75*, 125303.
[67] W.-K. Wang, Y.-J. Xu, S.-Y. Huang, K.-F. Liu, P.-C. Tsai, *Coatings* **2019**, *9*, 469.
[68] J. Liu, J. Wang, C. Xu, H. Jiang, C. Li, L. Zhang, J. Lin, Z. X. Shen, *Adv. Sci.* **2018**, *5*, 1700322.
[69] J. Li, J.-F. Gao, Z.-H. He, F.-F. Li, L.-B. Kong, *Ionics* **2021**, *27*, 4153.
[70] J. Yu, G. Xiong, S. Yin, X. Guan, H. Zhou, J. Xia, Y. Yang, S. Zhang, Y. Xing, P. Yang, *J. Alloys Compd.* **2023**, *934*, 168038.
[71] S. Hansen, F. Hahn, H. Krueger, F. Hoffmann, M. Andresen, R. Rainer Adelung, M. Liserre, *IEEE Power Electron. Mag.* **2021**, *8*, 60.
[72] S. Hansen, E. Quiroga-González, J. Carstensen, R. Adelung, H. Föll, *J. Power Sources* **2017**, *349*, 1.
[73] H. M. Rietveld, *J. Appl. Crystallogr.* **1969**, *2*, 65.
[74] A. A. Coelho, *J. Appl. Crystallogr.* **2018**, *51*, 210.
[75] R. W. Cheary, A. A. Coelho, J. P. Cline, *J. Res. Natl. Inst. Stand. Technol.* **2004**, *109*, 1.